NMR Solution Structures of the Apo and Peptide-Inhibited Human Rhinovirus 3C Protease (Serotype 14): Structural and Dynamic Comparison†

Trent C. Bjorndahl,‡ Lena C. Andrew,‡ Valentyna Semenchenko,§,|| and David S. Wishart*,‡,§,||

Faculty of Pharmacy and Pharmaceutical Sciences and Departments of Computing Science and Biological Sciences, University of Alberta, Edmonton, Alberta, Canada, and National Institute for Nanotechnology, Edmonton, Alberta, Canada

Received June 4, 2007; Revised Manuscript Received September 7, 2007

ABSTRACT: The human rhinovirus (HRV) is a positive sense RNA virus responsible for about 30% of "common colds". It relies on a 182 residue cysteine protease (3C) to proteolytically process its single gene product. Inhibition of this enzyme in vitro and in vivo has consistently demonstrated cessation of viral replication. This suggests that 3C protease inhibitors could serve as good drug candidates. However, significant proteolytic substrate diversity exists within the 110+ known rhinovirus serotypes. To investigate this variability we used NMR to solve the structure of the rhinovirus serotype 14 3C protease (subgenus B) covalently bound to a peptide (acetyl-LEALFQ-ethylpropionate) inhibitor. The inhibitor-bound structure was determined to an overall rmsd of 0.82 Å (backbone atoms) and 1.49 Å (all heavy atoms). Comparison with the X-ray structure of the serotype 2 HRV 3C protease from subgenus A (51% sequence identity) bound to the inhibitor ruprintrivir allowed the identification of conserved intermolecular interactions involved in proximal substrate binding as well as subgenus differences that might account for the variability observed in SAR studies. To better characterize the 3C protease and investigate the structural and dynamic differences between the apo and bound states we also solved the solution structure of the apo form. The apo structure has an overall rmsd of 1.07 ± 0.17 Å over backbone atoms, which is greater by 0.25 Å than what is seen for the inhibited enzyme (2B0F.pdb). This increase is localized to the enzyme's C-terminal β-barrel domain, which is responsible for recognizing and binding proteolytic substrates. Amide hydrogen exchange dynamics revealed dramatic differences between the two enzyme states. Furthermore, a number of residues exhibited exchange-broadened amide NMR signals in the apo state compared to the inhibited state. The majority of these residues are associated with proteolytic substrate interaction.

A large number of different viruses (rhinoviruses, enteroviruses, coronaviruses, and respiratory syncytial viruses) are responsible for upper respiratory tract illnesses or "colds" (*1*). However, recent studies have confirmed that the human rhinovirus (HRV[1]) is actually responsible for about 25 to 35% of all adult colds (*2*). Although colds rarely result in mortality, their estimated economic impact, in the United States alone, is 40 billion dollars annually. Furthermore, the impact of these illnesses translates into an estimated 90 million days of restricted work activity and 45 million lost school days (*3*). This makes HRV one of the leading causes of human disease and morbidity. This highly variable member of the picornavirus family includes more than 110 known serotypes. This remarkable serotype diversity has hindered the development of a single cold vaccine (*4*).

HRV serotypes are grouped into two genera, rhinovirus A and rhinovirus B. The rhinovirus B genus includes serotype 14 (HRV14), which is one of the better studied rhinoviral serotypes. Rhinoviruses, as with most picornaviruses, produce a single 250 kDa gene product or polyprotein that contains all the structural and nonstructural proteins necessary for viral replication. Typically the polyprotein is divided into three distinct regions (P1, P2, and P3). The P1 region contains the precursor viral capsid proteins while the P2 and P3 regions contain the precursors of functional proteins important for viral RNA replication. The majority of the proteolytic processing within P1, P2, and P3 is carried out by the 3C cysteine protease, which is a relatively small protein (21 kDa). In addition to viral proteolysis, the 3C protease is also responsible for host-cell "disabling" through selective proteolytic cleavage of host proteins (*5*). This deactivation is mediated by the virus's 3D gene product, a polymerase that binds the 3C protease and contains a nuclear localization sequence (NLS) that is used to transport the fused 3CD gene product to the host cell nucleus (*6*). Once inside

† This project was funded in part by the Protein Engineering Network Centres of Excellence (PENCE) and the National Sciences and Engineering Research Council of Canada (NSERC). T.C.B. was funded through the Rx&D/HRF scholarship and the Walter H. Johns Graduate Fellowship.

* Author to whom all correspondence should be addressed. Tel: (780) 492-0383. Fax: (780) 492-1071. E-mail: david.wishart@ualberta.ca.

‡ Faculty of Pharmacy and Pharmaceutical Sciences, University of Alberta.

§ Departments of Computing Science and Biological Sciences, University of Alberta.

|| National Institute for Nanotechnology.

[1] Abbreviations: HRV, human rhinovirus; HRV14-3C, human rhinovirus (serotype 14) 3C protease; NMR, nuclear magnetic resonance; DTT, dithiothreitol; EDTA, ethylenediamine tetraacetic acid; PFG, pulsed-field gradient; HSQC, heteronuclear single-quantum coherence; TOCSY, total correlation spectroscopy; NOESY, nuclear Overhauser enhancement spectroscopy; DSS, 2,2-dimethyl-2-silapentane-5-sulfonic acid; MALDI-TOF, matrix assisted laser desorption−time of flight; BMRB, BioMagResBank; PDB, Protein Data Bank.

10.1021/bi7010866 CCC: $37.00
Published on Web 10/18/2007

the nucleus, the 3C protease self-cleaves from the 3CD heterodimer and proceeds to cleave the host cell RNA polymerase (I, II, and III), poly(A)-binding protein, and transcription factors (*7*). Furthermore, the 3CD fusion protein has been shown to bind the viral RNA cloverleaf IRES I element (*8*) and is therefore implicated in viral RNA replication and translation.

These functions underline the 3C protease's central role in the rhinovirus life cycle, and because inhibition of this enzyme has shown to be effective at halting viral replication (*9*), 3C protease inhibitors have been investigated as potential pharmaceutical agents in treating some colds. However, despite significant efforts over the past 20 years to develop and structurally characterize inhibitors for this group of enzymes, only three X-ray crystal structures for the human rhinovirus 3C protease have been reported. These include structures for serotypes 2 (*9*), 14 (*10*), and 16 (*11*). However, only one coordinate data set, for an inhibitor-bound form of the HRV2-3C protease (PDB accession # 1CQQ), has ever been publicly released. These structural studies have shown that this 182 residue cysteine protease is composed of a two-domain, β-barrel structure similar to chymotrypsin-like serine proteases. The active site is situated between the two domains and consists of a cysteine-histidine-glutamate catalytic triad along with a proposed electrophilic oxyanion hole. A long, shallow grove in the C-terminal β-barrel domain accommodates a range of peptide substrates (*12*). Interestingly, cysteine proteases, unlike serine proteases, tend to recognize 4−5 residue cleavage sequences rather than single residues cleavage points (lysine/arginine for trypsin, hydrophobic residues for chymotrypsin). By convention, these substrate sequences are numbered as P for residues preceding the scissile bond and P′ for residues following the cleavage site. Residues from the P5 (the fifth residue preceding the cleavage site) to P'_3 (the third residue following the cleavage site) positions largely define the picornaviral 3C cleavage sequence. Studies by Cordingley et al. (*13*) initially determined a minimal substrate recognition sequence of six amino acids (TLFQ/GP). The HRV-3C proteases prefer a glutamine at the P_1 position, a glycine in the P'_1 position and exhibit a preference for a small, hydrophobic residue in the P4 position (*14*).

This information has been utilized to direct the development of various irreversible peptidyl 3C protease inhibitors including ruprintrivir (formerly AG7088). Interestingly, the structure−activity relationship studies done to date have shown noticeable serotype and subgenus diversity in substrate binding affinity and efficacy. Specifically, investigations into planar, hydrophobic residues in the substrate (S_2) binding pocket presented different inactivation rates for the 3C proteases for serotypes 14, 2, 10, 1A, 16, and 89 (*11*). These results were reiterated during irreversible-inhibitor optimization studies (*15*) and showed that hydrophobic moieties in the P_2 position were more favorable for serotype 14 proteases compared to serotypes 1A and 10. Furthermore, these studies reveal that leucine with its larger branched side chain is preferred in the P_3 position over valine for serotype 14, compared with serotypes 2 and 16.

To better understand this serotype diversity and to gain more insight into the mechanistic details of HRV-3C substrate recognition, binding, and catalysis we have used NMR to solve the solution structure of the HRV14-3C protease, both in its substrate-free (apo) and in its peptide-bound state (i.e., covalently linked to a natural peptide analogue of the 2C/3A cleavage sequence). This particular HRV (subgenus B) variant has 51% sequence identity to the HRV2-3C protease (subgenus A) whose X-ray crystal structure was solved with a bound peptide-mimic inhibitor. Comparison of the inhibitor-bound HRV-14 NMR structure with the HRV-2 X-ray structure has provided better understanding of the conserved components of the HRV-protease substrate binding mechanism. It has also provided new insights into the P_5 and P_6 recognition process and given more clarity regarding the deactivation of the enzyme via deamidation of Asn^{164}. Likewise, comparison between our inhibitor-bound HRV-14 and apo HRV-14 protease structures, determined under near identical solution conditions, allowed us to characterize key structural and multi-time scale dynamic differences between the apo and inhibitor-bound forms of the enzyme. Our results indicate that the apo form, over many different time scales, is significantly more flexible than the inhibitor-bound form. This is evident from comparisons between the chemical shift-determined order parameters, the backbone hydrogen exchange rates, and the number of resonances exhibiting intermediate exchange characteristics.

MATERIALS AND METHODS

Protein Expression and Purification. A pET-3a plasmid containing the HRV14-3ABC gene (a gift from M. N. G. James, University of Alberta) was transformed into *Escherichia coli* BL2 1 (DE3) pLysS cells via electroporation. Following initial growth in 1 L of Luria broth medium to an OD600 ∼ 0.8, the cells were pelleted at 23000*g*, washed with phosphate buffered saline (pH 7.0), resuspended in 250 mL of either ^{15}N or $^{13}C/^{15}N$ labeled minimal medium, and grown at 37 °C in a benchtop shaker-incubator. Following a 1 h recovery period, the cells were inducted with 1.6 mM isopropyl β-D galactopyranoside and protein expression was carried out at 25 °C for 12 to 14 h (*16*). Booster doses of ampicillin were given every 6 h to maintain plasmid presence. Following induction, the cells were harvested by centrifugation and resuspended in 40 mL of 50 mM Tris-HCl, 1 mM EDTA, 5 mM DTT at pH 8.8. The cells were then lysed *via* a freeze−thaw process (three 20 min cycles: −70 °C to 4 °C) aided with 8 mg of lysozyme. Cellular DNA was precipitated with successive drops of 10% aqueous polyethylenimine and subsequently pelleted via centrifugation at 32600*g* for 30 min. The supernatant was collected and passed over a 150 mL Q-Sepharose column pre-equilibrated at 4 °C with 50 mM Tris-HCl buffer at pH 8.8 to 9.0 at a rate of 3 mL/min. The HRV14-3C protein eluted shortly after the initial flow-through with greater than 90% purity (yields were ∼60 mg/L). Fractions containing HRV14-3C were pooled and dialyzed into phosphate buffer (pH 6.5, 15 mM DTT and 0.5 mM EDTA). In addition to these steps, the apo enzyme was further purified using a 50 mL BioGel-HA hydroxyapatite column. Elution of HRV14-3C was performed using a gradient of 40−175 mM K_2HPO_4. Fractions containing the HRV14-3C were pooled and dialyzed into phosphate buffer (pH 6.5, 15 mM DTT, 0.5 mM EDTA and 0.1 mM NaN_3).

Inhibitor Synthesis. To investigate the inhibitor-bound structure of HRV14-3C protease an irreversible peptidyl

inhibitor was designed and synthesized. The inhibitor structure was based on the modified 2C/3A cleavage sequence used for the development of a *p*-nitroaniline colorimetric assay (*17*) and the Michael acceptor ethylpropenoate group used for the development of the covalent inhibitor, AG7088 (*18*). Our six residue peptidyl ethylpropenoate inhibitor was synthesized in two steps. Briefly, an acetylated peptide (acetyl-L-(OtBu-Glu)-L-Ala-L-Leu-L-Phe-COOH) was prepared *via* Fmoc solid-phase peptide synthesis. It was then chemically coupled in solution to a L-[(Trt)-Gln]ethylpropenoate moiety that was synthesized based on methods described by Dragovich et al. (*18*). Complete synthesis details are provided in the supplemental information.

NMR Sample Preparation. Inactivation of the HRV14-3C enzyme was achieved by incubation at 25 °C with a 6-fold molar excess of the inhibitor and the excess inhibitor subsequently removed *via* dialysis. The inhibited [U-^{13}C/^{15}N] HRV14-3C protease sample was concentrated to ~0.75 mM *via* ultrafiltration using Amicon Ultra 15 filtration devices (5000 MWCO). The [U-^{13}C/^{15}N] apo HRV14-3C protease sample was concentrated to ~1.0 mM in the same manner. D_2O (10%) was added to each sample to maintain spectral lock, and 0.1 mM DSS was also added for chemical shift referencing (*19*). To collect ^{1}H/^{2}H exchange data, the [U-^{13}C/^{15}N] samples were exchanged into 99.6% D_2O buffer (20 mM KH_2PO_4, 15 mM DTT, 0.5 mM EDTA, and 0.1 mM NaN_3, pD 6.9) with 6 successive steps of volumetric dilution and subsequent concentration by ultrafiltration using Amicon Ultra filtration devices (5000 MWCO). This process was done at 25 °C and was completed in ~2.5 h. Prior to NMR data collection, the protein samples were transferred to either SHIGEMI microcell NMR tubes or Wilmad 5 mm thin-walled NMR tubes and sealed under argon.

NMR Data Collection and Chemical Shift Assignment. All experiments were done at 25 °C using Varian 500, 600, and 800 MHz INOVA spectrometers. The 500 MHz spectrometer was fitted with either a 5 mm HCN *z*-gradient pulsed-field gradient (PFG) room-temperature probe or a *z*-gradient PFG Varian cryogenic probe. The 600 MHz spectrometer was equipped with a 5 mm HCN *z*-gradient PFG room-temperature probe. The 800 MHz spectrometer was equipped with a 5 mm HCN *xyz*-gradient PFG cryogenic probe. All experiments were conducted using Varian ProteinPack or BioPack pulse sequences (VNMR v3.1c or VNMRJ) with the exception of the 2D ^{13}C/^{15}N F1/F2-filtered TOCSY, which was supplied by Leo Spyracopoulos, University of Alberta.

Chemical shift assignments for the inhibited enzyme were obtained from ^{15}N-HSQC, ^{13}C-HSQC, HNCA (*20*), HNCACB (*21*), CBCA(CO)NH (*22*), C(CO)NNH (*23*), HC(CO)NNH (*23*), HNCO (*24*), CCH-TOCSY (*25*), HCCH-TOCSY (*26*), and HNHA (*27*) spectra. Proton chemical shift assignments for the bound inhibitor were obtained from a 2D ^{13}C/^{15}N F1/F2-filtered TOCSY. All NMR experiments conducted on the inhibited enzyme were performed at 500 MHz. For the apo enzyme, the side-chain assignments built upon previously published data (*28*) with the acquisition of 2D ^{13}C-HSQC (*29*) and 3D CCH-TOCSY (*25*), HCCH-TOCSY (*26*), HC(CO)NNH, and C(CO)NNH (*23*) experiments. Assignments from the peptide inhibited form of the HRV14-3C protease were used to assist with the assignment of a number of hard-to-identify resonances.

NOE restraints were obtained from ^{15}N-NOESY-HSQC and ^{13}C-NOESY-HSQC (*30*) experiments collected on the [U-^{13}C/^{15}N]-labeled samples. The ^{13}C-NOESY-HSQC experiment (without WET water suppression) was repeated using samples exchanged into 99.6% D_2O to obtain cross-strand $^1H_\alpha - ^1H_\alpha$ NOEs. The ^{15}N-edited NOESY experiments used a τ_m of 75 ms, while all ^{13}C-edited NOESY experiments employed a τ_m of 100 ms.

Hydrogen exchange data for the apo HRV14-3C protease were acquired from a series of two-dimensional ^{15}N-HSQC spectra collected at 0, 38, 99, 172, 486, and 6580 min following H_2O to D_2O exchange of the ^{13}C/^{15}N-labeled sample. For the inhibited HRV14-3C protease, hydrogen exchange data were acquired from a series of two-dimensional ^{15}N-HSQC spectra collected on the [U-^{13}C/^{15}N]-labeled sample at 0, 156, 312, 1220, 2765, and 8702 min following H_2O/D_2O solvent exchange. The ^{13}C-NOESY-HSQC experiment was collected at 800 MHz, and the deuterium exchange data for the apo HRV14-3C protease was collected at 600 MHz. All other experiments were collected at 500 MHz. All spectra were processed with NMRPIPE (*31*) and analyzed with NMRVIEW (*32*).

Inhibited HRV14-3C Structure Determination. 1911 non-redundant, intra-protein NOE assignments (749 short range, 690 medium range, 472 long range) were derived from the ^{15}N-NOESY-HSQC and ^{13}C-NOESY-HSQC (*30*) experiments collected on the [U-^{13}C/^{15}N]-labeled sample. A total of 11 intrainhibitor NOEs were obtained from a 2D ^{13}C/^{15}N F1/F2-filtered NOESY experiment (*33*), and 76 protein-inhibitor NOE restraints were obtained from the 3D ^{13}C/^{15}N-filtered/F3-edited NOESY experiment (*34*). Selected strip plots from this experiment are provided in the Supporting Information. NOEs were calibrated using proton cross-peak intensities and binned with upper bounds of 3.0, 4.0, and 5.5 Å corresponding to strong, medium, and weak intensities respectively. All lower bounds were set to 1.8 Å. A total of 131 $^3J_{HNH\alpha}$ coupling constants were unambiguously determined from the HNHA spectrum and used to assign 131 phi (φ) angles. 126 psi (ψ) angles were predicted using TALOS (*35*) and SHIFTOR (*36*). Phi and psi angle restraints were assigned following initial structure calculations with NOE data alone. The χ_1 for His^{40} was assigned based on H_β to H_N and H_α NOE intensities. Hydrogen bonds were identified following analysis of a ^{15}N-HSQC spectrum collected on the [U-^{13}C/^{15}N] labeled HRV14-3C protease sample exchanged into 99.6% D_2O buffer. Hydrogen bond donors were assigned to amides still presenting signals in the first of the series of ^{15}N-HSQC spectra (collected ~2.5 h after initiating the deuterium exchange at 25 °C, pD 6.9). Eighty-seven intra-enzyme hydrogen bonds were identified from these deuterium exchange experiments. Hydrogen bonds were assigned limits of 1.5−2.5 Å for H_N to O distances and 2.5−3.5 Å for N to O distances. Hydrogen bond donors between the enzyme and its substrate were assigned following the NOE-derived structure calculations. Preliminary structures were calculated using the PARALLHDG nonbonded parameter set with XPLOR-NIH v2.10 (*37*) *via* the simulated annealing protocol in dihedral space using only NOE data. Center-weighted pseudo-atom corrections were used for ambiguous methylene and methyl proton NOE

distances. After preliminary structure generation, subsequent structure calculations incorporated both hydrogen bond and dihedral angle restraints. The number of steps in the simulated annealing protocol was increased (high-temperature steps = 24,000 at 1000 °K; cooling steps = 12,000; final temperature = 100 K) to improve convergence. Refinement for the top 50 structures was performed with CNS version 1.1 (*38*) using the RECOORD water refinement protocol (*39*). The PARALLHDG and OPLSX nonbonded parameter sets were employed for the simulated annealing and water refinement protocols respectively.

Apo HRV14-3C Structure Determination. Preliminary structures of the apo HRV14-3C enzyme were created with CYANA (*40*) using the inhibited HRV14-3C protease (PDB code 2B0F) as a starting template. The ^{15}N and ^{13}C-edited NOESY peak lists were partially assigned manually using NMRVIEW (*32*) and used to generate starting NOE restraint lists. These lists were subsequently refined by CANDID (*41*) and NOAH (*42*) during CYANA's calculation. The refined peak lists were fed back into NMRVIEW for manual confirmation. The final set of peak lists provided 1515 nonredundant NOE assignments (533 short range, 535 medium range, 447 long range) from the ^{15}N-NOESY-HSQC and ^{13}C-NOESY-HSQC spectra (*30*). NOEs were calibrated using proton cross-peak intensities and binned with upper bounds of 3.0, 4.2, and 5.5 Å corresponding to strong, medium, and weak intensities respectively. All lower bounds were set to 1.8 Å. A total of 64 hydrogen bond donors were assigned to amides still presenting signals in the first of the series of ^{15}N-HSQC spectra (collected ~2.5 h after initiating the deuterium exchange at 25 °C, pD 6.9). Limits of 1.5−2.5 Å for H_N to O distances and 2.5−3.5 Å for N to O distances were used for hydrogen bond restraints. Twenty-nine stereospecific assignments were made with HABAS during the CYANA simulated annealing structure calculations and incorporated into subsequent structure calculations. $^3J_{HNH\alpha}$ coupling constants were determined from the HNHA spectrum (*27*) and used to unambiguously assign 129 phi (φ) angles. One-hundred psi (ψ) angles that matched TALOS (*35*) and SHIFTOR (*36*) predictions and clustered in favorable regions of the Ramachandran plot following the initial structure calculation were also assigned. Limits of ±40° were applied to the dihedral restraints. These limits were inflated to ±60° for residues displaying weak signals in the HNHA spectrum to account for increased errors in the measured $^3J_{HNH\alpha}$ data. Phi (φ) and psi (ψ) angle restraints were incorporated into the structure calculation after the initial structures were generated with NOE data alone. The χ_1 angle for His^{40} and χ_1 and χ_2 angles for Glu^{71} were restrained to values obtained for the inhibited HRV14-3C protease (PDB code 2B0F), which are also consistent with observed angles for the apo and inhibited HRV2-3C protease (*9*, *10*), the apo Polio-3C protease (*43*), and the apo FMD-3C protease (*44*). Three hundred initial structures were calculated via the simulated annealing protocol (high-temperature steps = 24,000 at 1000 K; cooling steps = 12,000; final temperature = 100 K) using CNS v.1.1 (*38*). Center-weighted pseudo-atom corrections were used for ambiguous methylene and methyl proton NOE distances. Fifty of the lowest energy structures with were refined in explicit solvent using the RECOORD protocol (*39*). The PARALLHDG and OPLSX nonbonded parameter sets were employed for the simulated annealing and water refinement protocols respectively. The top 20 structures had no NOE violations >0.2 Å and no dihedral angle violations >5° and were deposited into the PDB under accession code 2IN2.

Hydrogen Exchange: Protection Factor (P_{factor}) Calculations. All ^{15}N-HSQC exchange spectra used to collect ^{1}H/^{2}H exchange rate data were processed with identical phasing and apodization functions. Peaks were autopicked and volumes calculated with NMRVIEW (*32*). To obtain deuterium exchange rates (k_{ex}) the ^{15}N-HSQC amide peak volumes were fit to the first-order exponential decay equation using XCRVFIT v4.0.9 (*45*):

$$V = V_o\, e^{-kt} \quad (1)$$

where V is the peak volume, k is the rate constant, and t is time. The protection factors (P_{factor}) for each residue were calculated by comparing the calculated exchange rate (k_{ex}) with the predicted random coil exchange rates (k_{rc}) where

$$P_{factor} = k_{rc}/k_{ex} \quad (2)$$

The random coil rates (k_{rc}) were calculated using the methods described by Bai (*46*) and corrected for temperature and pD differences (*47*).

RESULTS AND DISCUSSION

Inhibited HRV14-3C Chemical Shift Assignments. In total, 2038 of 2171 possible ^{13}C, ^{15}N, and ^{1}H assignments were obtained for 181 of 182 residues in HRV14-3C protease (94% complete). The complete set of ^{1}H, ^{13}C, and ^{15}N chemical shift assignments for the inhibitor and inactivated enzyme were deposited into the BioMagResBank under accession #6823. Backbone amide assignments were unattainable for Gly^1, Ser^{21}, Asn^{80}, Asn^{110}, and Gly^{154}, which occupy the N-terminal, loop, and turn regions. All possible side chain proton assignments for the bound ethylpropenoate inhibitor were obtained from the 2D ^{13}C/^{15}N F1/F2-filtered TOCSY experiment collected on the [U-^{13}C/^{15}N] labeled HRV14-3C sample in 99.6% D_2O.

Apo HRV14-3C Chemical Shift Assignments. The side-chain assignments for the apo HRV14-3C protease were added to the previously deposited backbone assignments under BMRB accession #5659 (*28*). Aromatic assignments were obtained from NOESY data during the apo enzyme's structure calculation. A few additions to the original backbone assignment data were made subsequent to the collection of the additional data. In all, 92% of all possible backbone shifts were obtained at the conditions described, which included 85% of $^1H_\alpha$, 83% of $^{13}C'$, 90% of ^1H_N, 88% of ^{15}N, 98% of $^{13}C_\alpha$, and 97% of $^{13}C_\beta$ chemical shifts. For the apo enzyme, 1817 of 2131 possible ^{13}C, ^{15}N, and ^{1}H assignments were obtained for 180 of 182 residues (83% complete). There were an increased number of unassignable amide backbone chemical shifts (9%) for the apo enzyme in comparison to the inhibited HRV14-3C. In addition, there was a lack of homogeneity in resonance intensity and line width seen in the ^{15}N-HSQC spectra (Figure 1) for the apo HRV14-3C enzyme. This indicates that conformational exchange at the intermediate time scale exists for the apo form of the enzyme. In contrast, the inhibited enzyme displayed general uniformity of signal intensity throughout its ^{15}N-HSQC spectrum.

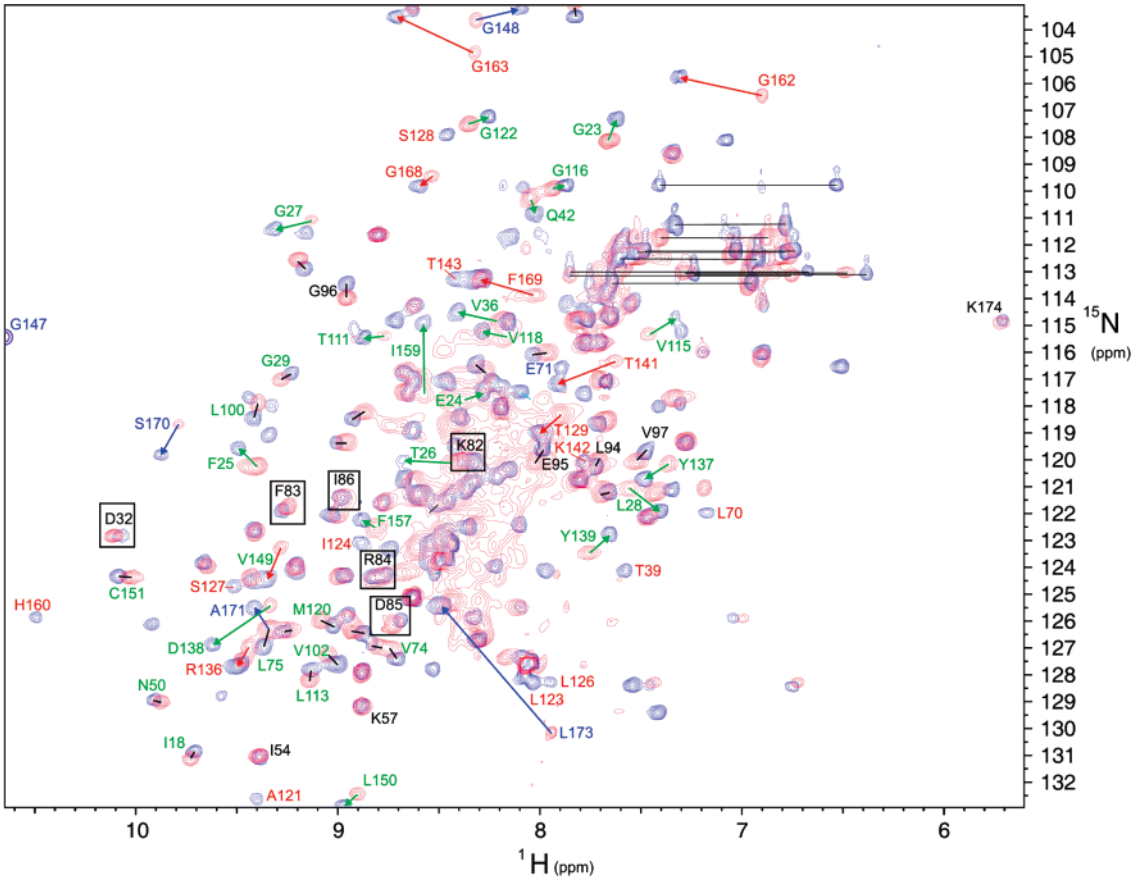

FIGURE 1: ^{15}N-HSQC spectra of the apo and acetyl-LEALFQ-ethylpropionate bound HRV14-3C protease. The ^{15}N-HSQC spectrum of the apo enzyme is colored red. The ^{15}N-HSQC spectrum of the inhibited enzyme is overlaid and colored blue. Peaks corresponding to residues in the RNA binding motif (KFRDI$^{82-86}$) are boxed and annotated black, and peaks corresponding to residues involved with direct inhibitor interaction are annotated red. Residues that show significant amide chemical shift changes are annotated blue and green. Blue annotated amide signals however, correspond with residues involved with interdomain contacts while signals annotated green are for residues involved with cross β-strand hydrogen bonds that make up the protein's extended dynamic network (Figure 6). The peak for Gly^{147} is not observed at this contour level and is drawn at its relative position.

The majority of these broad NMR signals are for residues associated with proteolytic substrate binding.

Enzyme Inhibition. The peptidyl-ethylpropenoate inhibitor used in these studies proved to be poorly water-soluble. As a result, cosolvents (dimethyl sulfoxide, water, and ethanol) were investigated to facilitate dissolution. Oxidation of the active site Cys^{146} in dimethyl sulfoxide was evident following a reduction of HRV14-3C protease activity in dimethyl sulfoxide/water cosolvents (data not shown). However, the protease activity was not significantly altered in as much as 10% ethanol/water. These results are consistent with earlier reports (*48*) that explored HRV14-3C enzyme activity in various solvents. Consequently, ethanol/water (33% v/v) was chosen as the initial solvent with the inhibitor concentration being 2.5 mM. After addition to the enzyme solution, the final ethanol concentration for the colorimetric assays and enzyme−inhibitor reactions did not exceed 2%. Covalent binding of the inhibitor was confirmed with the commercially available *p*-nitroanaline (pNA) colorimetric assay (*17*) both pre- and postdialysis. Comparison of MALDI-TOF mass spectra collected on both apo [U-^{13}C/^{15}N] HRV14-3C and inhibited [U-^{13}C/^{15}N] HRV14-3C samples confirmed the enzymatic results and covalent modification of the protease with a mass difference of 811 amu, which is within 5 amu for the inhibitor (816 amu). The observed experimental error resulted from comparing the difference in average masses between ^{13}C/^{15}N uniformly labeled protein samples and is within the mass accuracy of the instrument.

Inhibited HRV14-3C Structure. An average of 10.5 intraprotein NOEs per residue were obtained for the inhibited enzyme structure calculations. In total, 2.6 long-range NOEs per residue and 3.8 medium-range NOE restraints per residue yielded structures with good structural statistics and precision (Table 1). Six of the twenty deposited structures had a total of five NOE restraint violations greater than 0.2 Å. No restraints had violations exceeding 0.3 Å. AQUA (*49*) and PROCHECK-NMR (*50*) were used to calculate and analyze NOE and dihedral angle restraint violations. Geometric and structure quality analysis was carried out using VADAR (*51*) and WHAT-CHECK (*52*) following water refinement with RECOORD (*39*). PROCHECK analysis indicates that the solution structures have equivalent X-ray resolutions of 2.4Å based on Ramachandran plot quality assessment and 1.1 Å based on χ_1 pooled and χ_2 trans angle standard deviation assessments. The deposited structures had nearly 79% of their residues in the φ/ψ core region. Interestingly, Asp^{32} occupies a disallowed region of the Ramachandran plot (φ, 51 ± 5°; ψ, −91 ± 5°). Asp^{32} is positioned near the RNA binding motif KFRDI$^{82-86}$ and forms backbone hydrogen bonds with Phe^{83}. Other 3C enzymes within the picornaviridae family with solved structures (Polio-3C, Asp^{32}; HRV2-3C, Asp^{32}; HAV, Asp^{32}) also exhibit similar φ and

Table 1: Structural Statistics for the HRV14-3C Proteases

	inhibited	apo
distance restraints		
all NOE distances	1998	1515
intraresidue (protein) NOEs	1911	1515
sequential ($\|i-j\|=1$)	749	533
medium ($1<\|i-j\|\leq 4$)	690	535
long ($\|i-j\|\geq 5$)	472	447
interresidue (protein-inhibitor) NOEs	76	
intraresidue (inhibitor) NOEs	11	
hydrogen bonds	87	64
violations		
structures with violations >0.3 Å	0	0
structures with violations >0.2 Å	6	0
dihedral angle restraints		
all	258	231
φ	131	129
ψ	126	100
χ_1 and χ_2	1	3
Ramachandran plot[a]		
residues in most favored region	78.90%	79.40%
residues in additionally allowed region	19.90%	19.40%
residues in generously allowed region	0.50%	0.60%
residues in disallowed region	0.60%	0.60%
WHAT-CHECK scores[b]		
second generation packing	−1.25	−0.53
χ_1/χ_2	−1.74	−0.89
rmsd to mean structure (Å)[c]		
backbone	0.82 ± 0.13	1.07 ± 0.17
heavy atom	1.49 ± 0.20	1.56 ± 0.25
region 15−78		
backbone	0.72 ± 0.14	0.87 ± 0.22
heavy atom	1.41 ± 0.20	1.64 ± 0.31
region 99−103, 111−172		
backbone	0.56 ± 0.12	1.00 ± 0.21
heavy atom	1.17 ± 0.17	1.57 ± 0.25

[a] Calculated with PROCHECK-NMR (*50*). [b] Calculated with WHAT-CHECK (*52*). [c] Calculated with MOLMOL (*70*).

ψ angles around 48 ± 6° and −120 ± 7° respectively for this particular residue. This residue yielded $^3J_{HNH\alpha}$ coupling constants of 4.6 and 6.0 Hz for the inhibited and apo HRV14-3C enzyme respectively as well as weak $H_N-H_{N(i-1)}$ and strong $H_N-H_{\alpha(i-1)}$ NOEs.

The solution structure of inhibited-HRV14-3C (Figure 2) was solved with an overall backbone atom rmsd of 0.82 ± 0.13 Å and a heavy atom rmsd of 1.49 ± 0.20 Å (residues Gly[1] to Glu[180]). A larger rmsd over the termini, domain linker (Asn[80]−Gly[96]), and loop regions (residues Asp[64]−Ile[68] and His[104]−Asn[110]) skewed the global rmsd to larger values compared with the β-barrel domains alone. The C-terminal β-barrel (Ala[99]−Leu[173]) is involved with the inhibitor binding and provided a slightly tighter rmsd (0.56 ± 0.12 Å for backbone atoms and 1.17 ± 0.17 Å for all heavy atoms) compared with the N-terminal β-barrel formed between residues Ile[15] and Asp[78] (0.72 ± 0.14 Å for backbone atoms and 1.41 ± 0.20 Å for all heavy atoms). Twenty low-energy structures presenting good geometry, no improper or dihedral angle violations >5°, no bond-length violations >0.05 Å, and no NOE violations >0.3 Å were selected and deposited in the PDB under accession code 2B0F.

Analysis of medium and long-range NOE patterns (*53*), $^3J_{HNH\alpha}$ coupling constants (*54*, *55*), and chemical shifts (*56*) confirmed α-helical secondary structure for residues Pro[2]−Lys[12] (**A**) and Thr[39]−Ala[41] (**B**) and β-strand secondary structure for residues Ile[15]−Thr[20] (**Ia**), Glu[24]−His[31] (**Ib**), Val[34]−Ile[37] (**Ic**), Asp[46]−Leu[48] (**Id**), Gln[52]−Asp[64] (**Ie**), Leu[72]−Arg[79] (**If**), Ala[99]−Val[103] (**IIa**), Val[115]−Leu[126] (**IIb**), Pro[130]−Arg[136] (**IIc**), Val[149]−Ala[152] (**IId**), Lys[155]−Gly[163] (**IIe**), and Arg[166]−Gln[172] (**IIf**). These elements are folded into two six-stranded β-barrel domains (Figure 2) that accommodate the active site residues, His[40], Glu[71], and Cys[146] in a shallow cleft. The RNA binding site, KFRDI[82−86], is capped by a short helix (Arg[87]−Phe[89]) and resides in a random coil region that tethers the β-barrel domains. This coil resides on an opposite side of the protein relative to the proteolytic site. These structural elements are conserved among all the picornaviridae 3C protease structures reported to date.

The domains of the HRV14-3C protease overlay with those from the HRV2-3C protease with backbone rmsd values of ∼0.98 Å for the N-terminal β-barrel domain (residues 1−80) and ∼1.05 Å for the C-terminal β-barrel domain (residues 111−178). The global backbone rmsd between the average NMR HRV14-3C structure and the X-ray structure for HRV2-3C is ∼1.24 Å when the domain linker (Asn[80]−Ala[99]) is not included in the calculation. Sequential and structural diversity exists between the two serotypes in the region following the RNA binding site (KFRDI[81−86]) that inflates the global rmsd to ∼2.67 Å when this region is included in the rmsd calculation. This coil intersects two important regions of the enzyme that interact with viral RNA (KFRDI[81−86]) and the viral 3D polymerase (TGK[153−155]). However, any significant differences between the serotypes in regard to their sequences and structures that might result remain unclear. No differences with respect to domain orientation exist between the two superposed inhibited enzymes.

Inhibitor−HRV14-3C Interactions. The substrate used in this study involved six naturally occurring residues (LEALFQ) in contrast to the four peptide-mimic residues incorporated in ruprintrivir, which was used to inhibit the HRV2-3C protease. This allowed for a detailed comparison of the proteolytic binding site between these two serotypes. In addition to proximal proteolytic interactions, the added length of our inhibitor allowed for characterization of interactions between the enzyme and substrate P_3 to P_6 residues. A schematic representation of these interactions is shown in Figure 3, and a comparison between the two different inhibitors in their bound conformation is shown in Figure 4. A discussion of these interactions in sequential detail follows beginning with the substrate P_1 and the HRV14-3C enzyme interactions.

Substrate P1−Enzyme Interactions. The specificity of the HRV14-3C protease for a glutamine residue in the P1 position has been previously demonstrated. The three hydrogen bonds that are observed between ruprintrivir's pyrrolidine and the HRV2-3C protease are mimicked in our peptidyl inhibitor bound to the HRV14-3C protease. The backbone amide of the inhibitor's P_1 glutamine acts as a hydrogen bond donor to the carbonyl of Val[161]. The side chain of the P_1 glutamine makes a number of van der Waals contacts by filling a shallow cleft between the **IIe** β-strand and the coil region formed between residues Thr[141] to Gly[144]. The P_1 glutamine positions its side chain amide to form three key hydrogen bonds. One hydrogen bond extends from its side-chain carbonyl to the $H_{\epsilon 2}$ of His[160]. The other two hydrogen bonds are formed from its side-chain amide protons

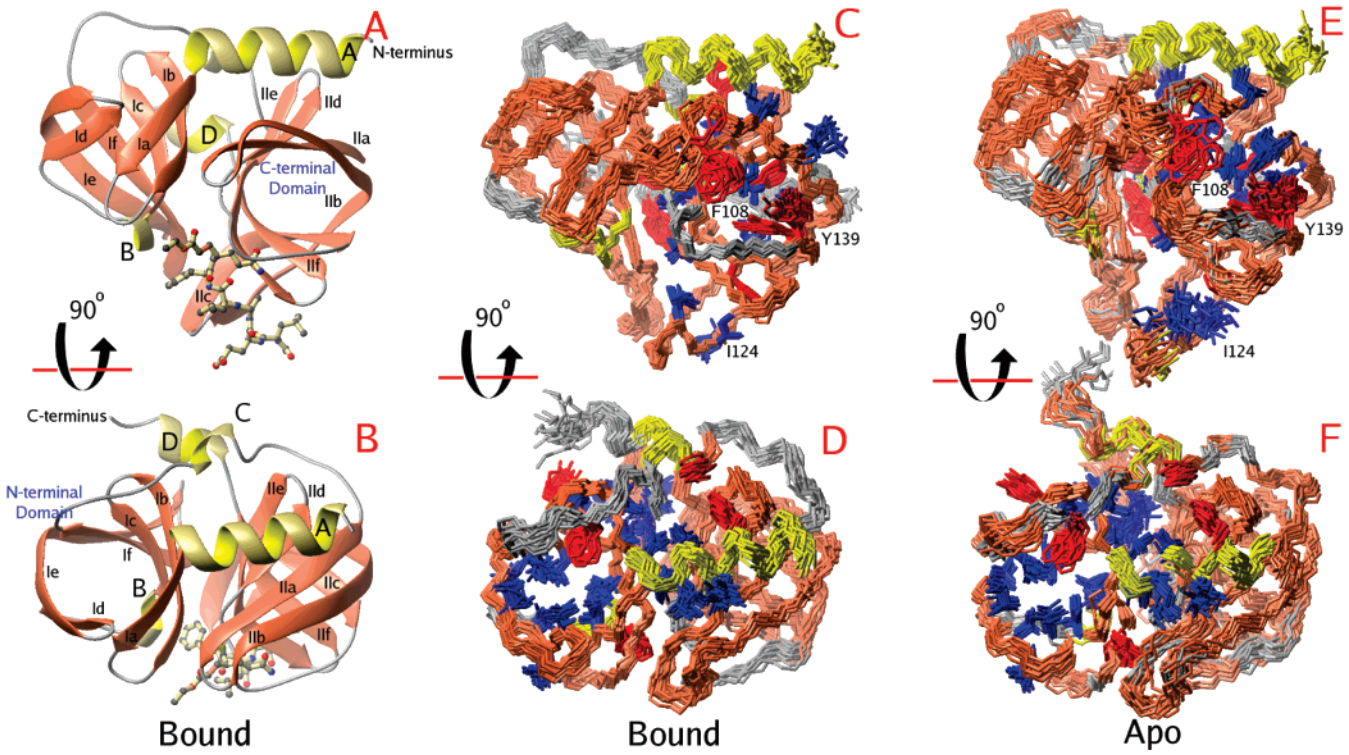

FIGURE 2: (A, B) Ribbon representation of the inhibited HRV14-3C protease. α-Helices are colored yellow and labeled with capital letters. β-Strands are colored orange and labeled with lowercase subscript. The N-terminus β-barrel domain has the prefix I, and the C-terminus β-barrel has the prefix II. B is rotated 90° about the *x*-axis with respect to representation A. The acetyl-LEALFQ-ethylpropionate inhibitor is rendered as a ball and stick figure. (C) Structural ensemble of the HRV14-3C protease with the C-terminal β-barrel domain superposed. (D) Structural ensemble of the HRV14-3C protease with the N-terminal β-barrel domain superposed. Representations E and F depict similar ensembles as C and D but for the apo enzyme. A larger backbone rmsd is observed for residues in the C-terminal β-barrel domain.

to the backbone carbonyl and side-chain hydroxyl groups of Thr[141]. Differences between the inhibitors in this position result in a slight differences in the φ angle for a conserved threonine residue (HRV14-3C, Thr[141] $-114 \pm 15°$; HRV2-3C, Thr[142] $-57°$).

Substrate P2− Enzyme Interactions. The S_2 pocket is a large, negatively charged cleft between the two β-barrel domains. Despite the negative electrostatic charge that results from the presence of the active site Glu[71] in the back of the pocket, a number of synthetic inhibitors have incorporated aromatic and poly-aromatic rings at the P_2 position with favorable results (*11*). The phenylalanine residue incorporated in our inhibitor bound to the HRV14-3C protease in a similar fashion compared to the fluoro-substituted aromatic ring incorporated within AG7088 bound to the HRV2-3C protease. The aromatic ring in this substrate position significantly reduces the protein's solvent accessible surface area by making numerous van der Waals contacts with the enzyme (His[40], Asn[69], Glu[71], Leu[126], Ser[127], Thr[129], and Thr[131]).

Variable P_2 substrate recognition exists between the rhinoviral 3C proteases whereby subgenus B serotypes prefer more hydrophobic groups in this position (*57*). This diversity possibly stems from the neutral to charged residue substitution observed in this pocket on the N-terminal β-barrel domain. The neutral residues, Gln[42] and Asn[69], found in subgenus B rhinoviruses differ from the charged residues, Asp[42] and Lys[69], found in subgenus A rhinoviruses. These changes affect the electrostatic surface of the binding pocket and may account for the increased substrate recognition that the HRV14-3C protease demonstrates when hydrophobic groups are incorporated in the P_2 position.

Substrate P3−Enzyme Interactions. Antiparallel β-strand hydrogen bonds are formed between the backbone atoms of the inhibitor's P_3 residue and the enzyme's Gly[163] residues. The P_3 leucine side chain is directed toward the solvent and covers the substrate binding pocket spanning the P_1 and P_2 residues of the inhibitor. The HRV14-3C protease demonstrates a preference for a larger branched-chain amino acid (leucine) in the P_3 position, in contrast to the smaller branched-chain amino acid (valine) preferred for other rhinovirus serotypes (*64*). This larger residue was incorporated in our inhibitor to help analyze this difference. Subgenus diversity appears to stem from van der Waals contacts existing between the δ methyl group of the P_3 leucine and the γ methyl group of Thr[143]. A threonine residue is found in the subgenus B rhinovirus 3C proteases, whereas this residue is substituted for the smaller amino acid, serine, in subgenus A rhinovirus 3C proteases (*65*). The leucine residue is sufficiently large enough to span the entire S_3 pocket and make contact between the P_1 glutamine and P_2 phenylalanine residues.

Substrate P4−Enzyme Interactions. The P_4 position marks the point where significant differences emerge between ruprintrivir and our "natural" inhibitor with respect to their structure and binding orientation. Our study indicates that the backbone atoms of the P_4 residue bridge the **IIb** β-strand and form hydrogen bonds with the backbone amide of Ser[127] and the backbone carbonyl of Asn[125]. The methyl group of the alanine in the P_4 position is tucked inside the S_4 binding pocket and makes contact with the $^1H_\alpha$ protons of Gly[163] and the aromatic protons of Phe[169]. The specificity for a small residue is understandable as the side chain is oriented inward

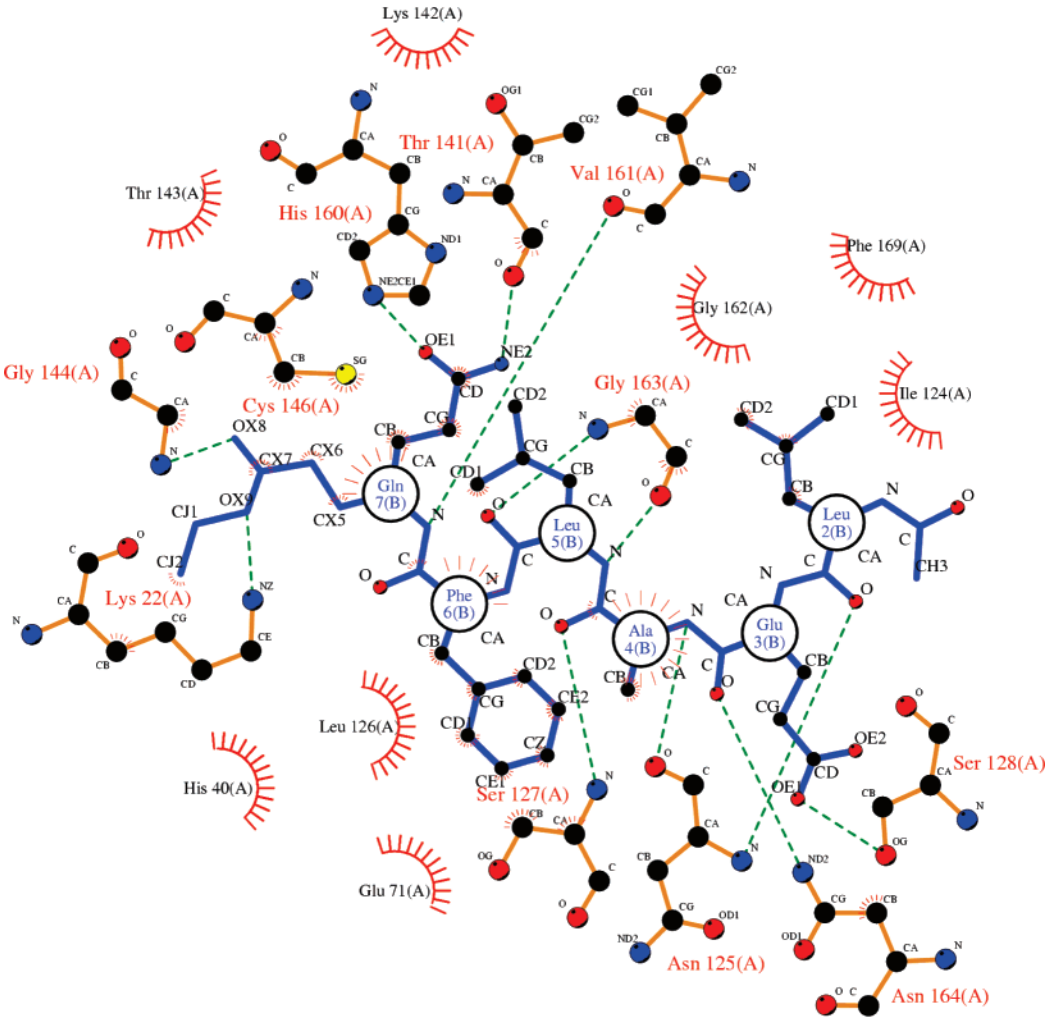

FIGURE 3: The network of hydrogen bonds between the peptide substrate (segment B) and the enzyme depicts an antiparallel β-strand formation for residues P_2 to P_6 (represented as broken lines). Other key hydrogen bonds and van der Waals contacts with conserved HRV-3C residues are also shown. The covalent bond between Cys^{146} and the CX5 carbon of the inhibitor is not shown. The schematic representation was created with LIGPLOT (*71*).

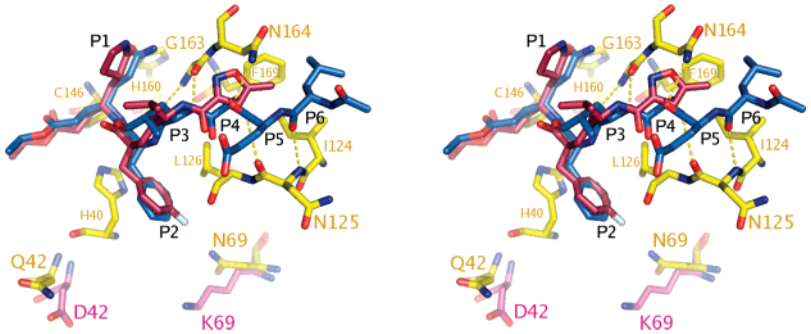

FIGURE 4: Wall-eyed stereo image of superposed bound HRV-3C protease inhibitors. The acetyl-LEALFQ-ethylpropionate inhibitor is colored blue and annotated from the P_1 to the P_6 substrate positions. Ruprintrivir is colored red. Residues within the HRV14-3C protease are colored yellow, and residues within the HRV2-3C protease are colored pink. The image was created with PyMOL (*62*).

and fills the shallow substrate binding pocket. In contrast to our "natural" substrate, the isoxazole ring incorporated in ruprintrivir is flipped 180° compared to the P_4 alanine such that the nitrogen and oxygen atoms within the ring are involved in interactions with Gly^{164}'s backbone carbonyl and Asn^{165}'s side chain in the **IIe** β-strand rather than hydrogen bonding to residues in the **IIb** β-strand.

Substrate P5 and P6−Enzyme Interactions. No residue specificity for the P_5 amino acid has yet been identified. This is understandable because this residue is solvent exposed. The glutamic acid residue used in our inhibitor is oriented parallel to the **IIb** β-strand backbone, makes van der Waals contacts with the side chain of Asn^{125}, and forms a hydrogen bond with the hydroxyl of Ser^{128}. The backbone carbonyl of the P_6 residue acts as a hydrogen bond acceptor for the backbone Asn^{125} amide. The side chain of the P_6 leucine is directed away from P_5 side chain and fills the remainder of the binding pocket below Asn^{164} making numerous van der Waals contacts with the aromatic ring of Phe^{169} and the side chain of Ile^{124}. These hydrophobic contacts explain the

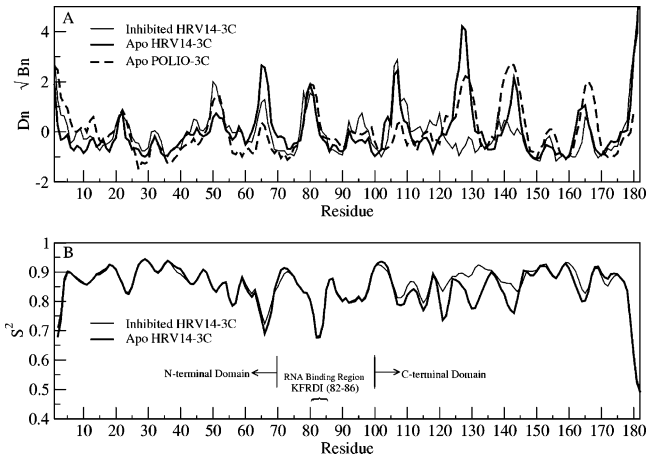

FIGURE 5: Atomic displacement and order parameter plots. (A) The normalized atomic displacements (D_n) for two states of the HRV14-3C protease (apo and inhibited) are compared with the normalized *B*-factors (B_n) for the homologous apo Polio-3C protease. (B) Chemical shift derived order parameters (S^2) for the apo and inhibited HRV14-3C protease.

serotype conservation of these 3C protease residues (*58*) and the preference for a hydrophobic residue in this position.

Substrate cleavage studies have demonstrated that inclusion of the P_5 residue results in a 4-fold increase in substrate recognition, while inclusion of the P_6 to P_8 residues increases substrate cleavage a further 2-fold (*24*). Analysis of this phenomenon with our substrate was conducted with the program STC (*59*), which revealed that elimination of the P_6 leucine residue increased the enzymes nonpolar solvent accessible surface area by ~45 ± 15 Å^2 and reduced the predicted K_D by 24 ± 5-fold. These results support the experimental observations that shortened substrates have impaired recognition (*14*).

Substrate−Asn^{164} Interactions. HRV14-3C's Asn^{164} residue is incorporated within a β-turn between the **IIe** and **IIf** β-strands. Our study indicates that the Asn^{164} side chain is important for forming key hydrogen bonds with the P_5 backbone atoms and contributing to the antiparallel binding orientation of the substrate. Because the side chain of Asn^{164} is solvent exposed, no direct observation of NOEs between the inhibitor and enzyme's Hϵ protons was possible. Consequently our structure calculations produced two primary χ_2 angle orientations for Asn^{164} (−90 ± 2° or 33 ± 2°). The χ_1 angle, however, was consistently found to be 174 ± 7°. The two χ_2 orientations direct Asn^{164}'s side-chain amide toward either the P_5 or its own backbone carbonyl. The latter orientation allows for an electrostatic interaction between the Asn^{164} side-chain amine and the P_5 backbone carbonyl. This interaction, however, positions Asn^{164}'s side-chain carboxylate and backbone carbonyl groups within 3 Å of each other. The former orientation, however, allows for the formation of two hydrogen bonds between Asn^{164} 's side chain amide and its own backbone carbonyl and between its side-chain carbonyl and the P_5 residue's backbone amide. The significance of this interaction is apparent from the 10-fold reduction in binding affinity upon deamidation of Asn^{164} (*60*). It is still not known if the deamidation mechanism is host-cell mediated, autocatalytic, or a nonenzymatic event. It is known that having a glycine following an asparagine residue

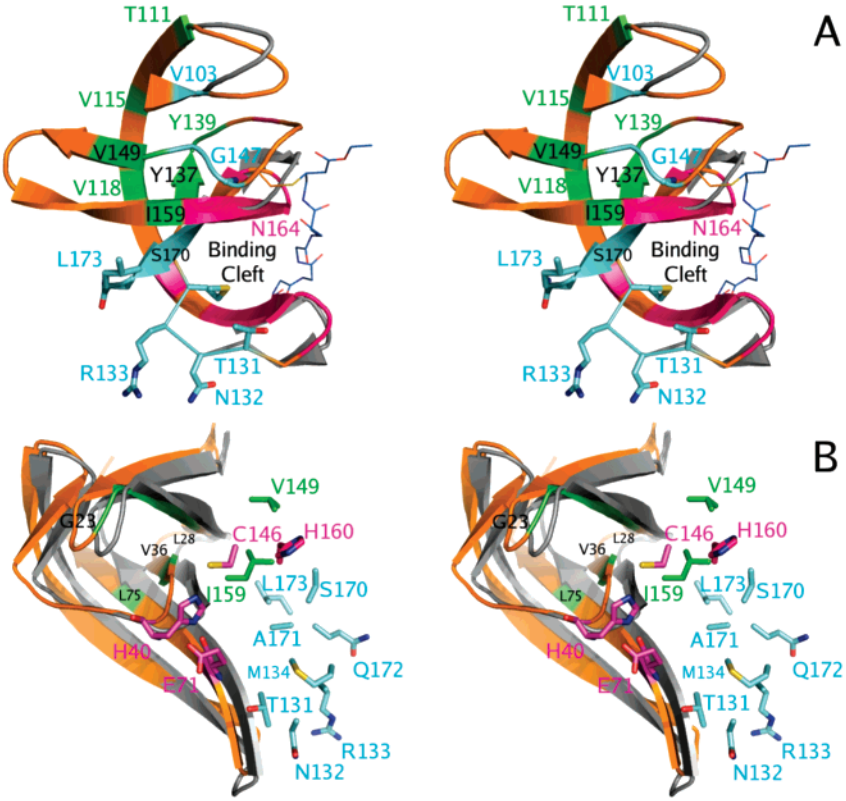

FIGURE 6: Shown are wall-eyed cartoon representations for portions of the C-terminal β-barrel domain for the apo (gray) and inhibited (gold) HRV14-3C protease. The ribbon is colored magenta for residues that interact with the inhibitor directly, green for residues that display primarily amide chemical shift changes upon inhibitor binding, and blue for residues that show chemical shift changes for atoms other than amides alone. The backbone of the inhibitor is shown as a stick figure, and the binding cleft is labeled for spatial comparison. A ribbon for the C-terminal β-barrel is shown in panel A and for the N-terminal β-barrel in panel B.

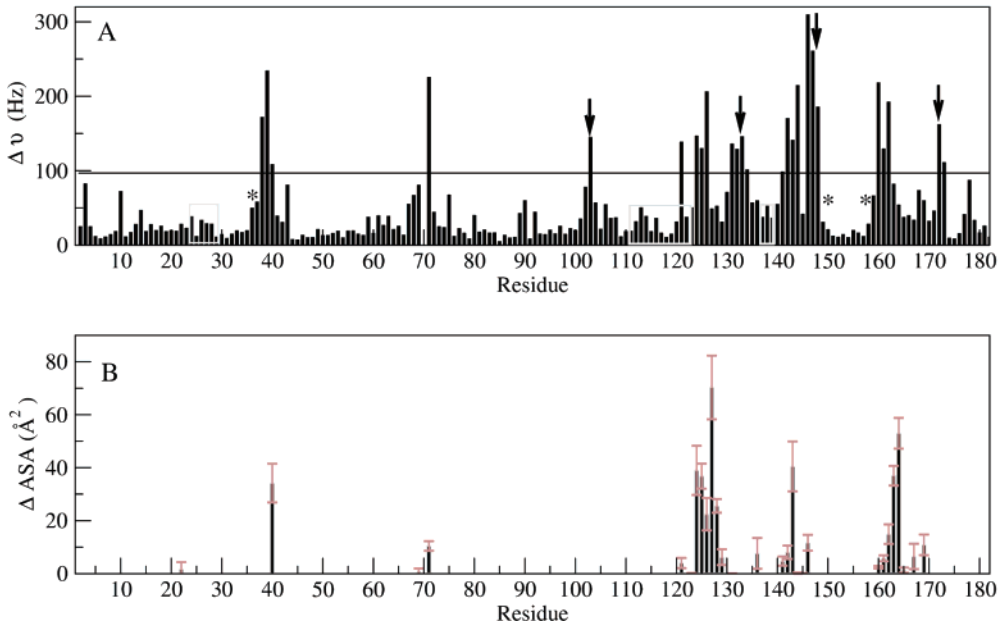

FIGURE 7: (A) All atom chemical shift changes. Chemical shift changes were calculated with CSDIFF (http ://www bionmr com/csdiff) using the formula $|v_{HN1} - v_{HN2}| + |v_{N1} - v_{N2}| + |v_{C'1} - v_{C'2}| + |v_{C\alpha1} - v_{C\alpha2}| + |v_{C\beta1} - v_{C\beta2}|$/number of atoms used. The line indicates twice the mean chemical shift perturbation value. Residues exhibiting amide chemical shift perturbations (Figure 1) are boxed and marked with an asterisk. Arrows mark residues that presented significant chemical shift perturbations that could not arise from inhibitor interactions. (B) Accessible surface area changes. Surface area changes upon inhibitor binding for the HRV14-3C protease (PDB code 2B0F) were calculated with STC (*59*).

can facilitate a spontaneous deamidation event of asparagine residues (*68*). Regardless of the exact mechanism, the impact this deamidation event has on substrate recognition and, therefore, possible autoregulatory mechanisms are evident. It is noteworthy that a number of other 3C proteases have conserved Asn-Gly sequences, including HRV2-3C, Polio-3C, and FMD-3C. However, to date this reaction has not been investigated nor has it been characterized in any other 3C protease.

This interaction is markedly different in the X-ray structure of the ruprintrivir-bound HRV2-3C, in which the inhibitor's isoxazole ring occupies the S_4 pocket and sits orthogonal to the **IIe** β-strand. To accommodate this orientation, the residues within the β-strand are pushed upward and do not take on typical β-turn φ and ψ and angles. Furthermore, HRV2-3C's Asn^{165} adopts χ_1 and χ_2 angles of 60° and 30° respectively to allow hydrogen bonds to form with the isoxazole ring. In contrast, the HRV14-3C protease forms well-defined type II′ β-turn backbone torsion angles when interacting with the natural peptide substrate.

Apo HRV14-3C Structure. As noted earlier, the determination of the apo-HRV14-3C structure was undertaken to better understand the conformational and dynamic changes that occurred upon substrate binding. For this particular structure we used an average of 8.5 NOEs per residue for the structure calculations. Approximately 2.5 NOEs per residue were used for long-range restraints and 3.5 NOEs per residue were medium-range restraints. The final structures had good structural statistics and precision (Table 1). None of the deposited structures had violations greater than 0.2 Å. The total number of NOEs used in the structure calculation was lower than that used for the inhibited HRV14-3C structure (2B0F.pdb), however, the resulting structures were statistically comparable because the majority of the unassigned NOEs were sequential and provided minimal contribution to the overall structure calculation and global fold. In addition, the ^{13}C-edited NOESY data collected on the apo HRV14-3C was collected at 800 MHz and the data collected on the inhibited HRV14-3C was collected at 500 MHz. The increased field strength provided better resolved NOE peaks with less spectral overlap and subsequently improved restraint calibration. These factors resulted in improved resolution, which provided better refinement of the Glu^{95}−Ala^{99} region in the apo structures compared with the inhibited form. This particular region flanks the RNA binding region and has been implicated with viral 3D polymerase interactions. The overall backbone rmsd of the apo HRV14-3C structures is 1.07 Å. The N-terminal β-barrel domain superposes with a smaller rmsd (0.87 Å) compared to the C-terminal β-barrel domain (1.00 Å), which is involved with proteolytic substrate recognition. The regions of the enzyme that inflated the rmsd values are located at Lys^{61}−Leu^{72}, Ser^{105}−Asn^{110}, and Leu^{123}−Ile^{135}. All of these loop/turn regions are involved with proteolytic substrate interaction and are presumed to undergo conformational exchange processes at the intermediate time scale (Figure 1). These

Table 2: Superposition of Picornaviridae 3C^{Pro} RNA Binding Region

protease	PDB code	superposed RNA region	pairwise fit (Å)[a]
HRV14-3C[b]	2IN2	HD$^{31-32}$ KFRDI$^{82-86}$ I^{156}	0.28
HRV2-3C[c]	1CQQ	YD$^{31-32}$ KFRDI$^{82-86}$ I^{157}	0.51
POLIO3C	1L1N	HD$^{31-32}$ KFRDI$^{82-86}$ I^{157}	0.63 ± 0.13
HAV-3C	1HAV	KD$^{35-36}$ KFRDI$^{95-99}$ I^{187}	0.57 ± 0.06
HAV-3C[c]	1QA7	KD$^{35-36}$ KFRDI$^{95-99}$ I^{187}	0.61 ± 0.03
HAV-3C[c]	2AO4	KD$^{35-36}$ KFRDI$^{95-99}$ I^{187}	0.51
HAV-3C[c]	2CXV	KD$^{35-36}$ KFRDI$^{95-99}$ I^{187}	0.29
FMD-3C	2BHG	FG$^{37-38}$ KVRDI$^{95-99}$ I^{177}	0.44 ± 0.40

[a] Backbone heavy atom pairwise fits to 2B0F.pdb. Calculated with MOLMOL (*70*). [b] Comparison between mean NMR structures. [c] Structures with bound inhibitors.

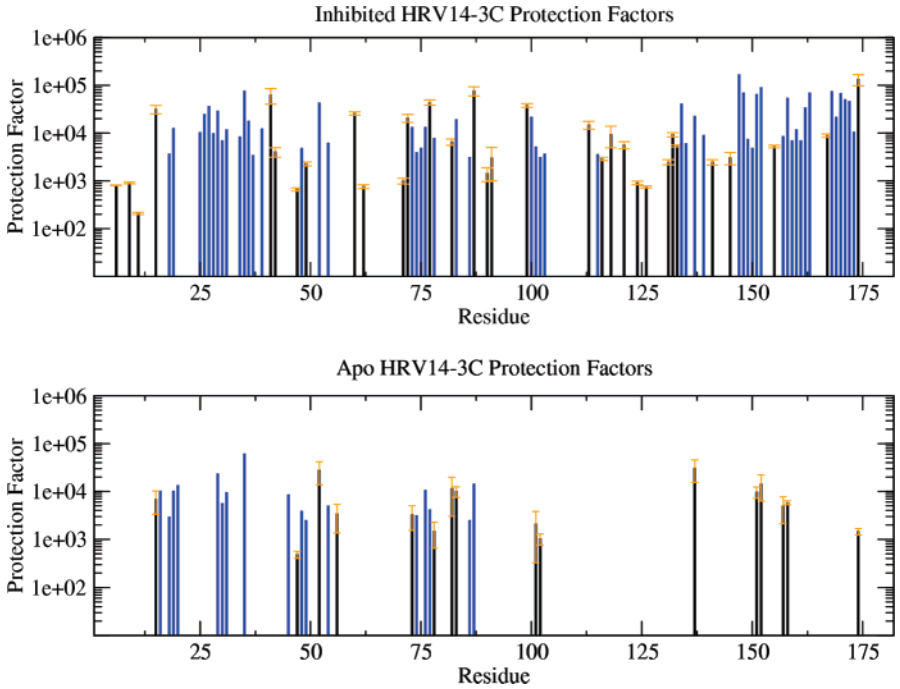

FIGURE 8: Apo vs bound P_{factor} data. The apo form of the HRV14-3C protease exhibits a substantial increase in deuterium exchange for residues occupying the C-terminal β-barrel domain. No measurable k_{ex} rates could be calculated except for residues either involved with or proximal to the RNA binding site (*67*). Protection factors for residues presenting amide exchange within the experimental time frame are colored black with orange error bars. Protection factors for residues that did not completely exchange during the experimental time frame were calculated with the maximum allowed k_{ex} of 8.0×10^{-4} and 1.0×10^{-3} for the inhibited and apo enzymes respectively. These data are colored blue and do not have error bars.

regions also presented fewer chemical shift and NOE assignments compared to the rest of the protein.

Structural Comparison between the Apo and Inhibited HRV14-3C Proteases. The average apo HRV14-3C protease (2IN2.pdb) superposes with the average inhibited HRV14-3C protease (2B0F.pdb) with a global rmsd of 0.69 Å when calculated with P*y*Mol (*62*). Superposition of the N-terminal β-barrel provided a tighter fit of 0.41 Å compared to the C-terminal β-barrel domain with a calculated rmsd of 0.73 Å. The increase in rmsd value for the C-terminal β-barrel domain results from regions that are involved with proteolytic substrate recognition. These regions also present larger atomic displacement values in the homologous (49% sequence identity) apo Polio-3C protease X-ray structure. The normalized *B*-factors for the apo Polio-3C structure were compared with the normalized rmsd values (*63*, *64*) for both the apo and inhibited HRV14-3C protease (Figure 5). A strong correlation exists between the homologous apo enzymes. An increase in atomic displacement is observed for residues involved with proteolytic substrate interaction for both of the apo enzymes ($Ile^{124}-Thr^{131}$ and $Arg^{136}-Gly^{147}$). However, once inactivated, these residues display reduced rmsd values and provide well-resolved amide peaks in the ^{15}N-HSQC spectrum (Figure 1). The loop regions around $Lys^{61}-Asn^{67}$ and $Val^{103}-Thr^{111}$ produced larger rmsd results in both the apo and inhibited HRV14-3C enzymes compared with the Polio-3C enzyme. The region $Val^{103}-Thr^{111}$ has been implicated in postscissile substrate binding and is not involved with substrate interactions for the inhibited solution structure (2B0F.pdb).

B-factors and rmsd displacements can be regarded as measures of shorter time scale dynamics (picoseconds to nanoseconds). Another useful measure of flexibility or dynamics is the order parameter. Typically smaller order parameters (<0.8) indicate regions of greater flexibility and disorder with the time scale for these measurements typically ranging from nanoseconds to microseconds. Recently a very simple approach to calculating order parameters from chemical shift data has been developed called the Random Coil Index (*65*). In Figure 5B these chemical shift-derived order parameters are compared between the inhibited and bound form of HRV14-3C protease. These data illustrate the generally smaller order parameters found throughout proteolytic substrate binding site in the apo form of the enzyme (relative to the inhibited enzyme). These differences appear to track quite well with the atomic displacement values and *B*-factors plotted in Figure 5A.

In order for the 3C enzyme to recognize and bind its various natural substrates local conformation changes within the substrate binding interface must occur. A general closure around the substrate is observed in the average NMR structures upon inhibitor binding (Figure 6). A number of amide chemical shift perturbations are observed in the ^{15}N-HSQC spectrum (Figure 1) that do not correspond with direct interaction of the inhibitor (annotated green and blue). Specific residues that display only amide chemical shift changes and are observed up to three β-strands away from any direct interaction with the inhibitor (Leu^{75}, Val^{115}, Val^{118}, and Leu^{150}) reiterate the sensitivity of amide chemical shifts to hydrogen bond lengths (*66*) and indicate that slight flexure of the C-terminal β-barrel occurs upon inhibitor interaction.

To investigate if structural changes occur in the other areas of the protease following inhibition, the protein's solvent accessible surface area changes were compared with chemical shift perturbations for all available atoms (BMRB entry 5659 vs BMRB entry 6823) upon inhibitor interaction (Figure 7).

This chemical shift data is more sensitive to backbone torsion angles and could potentially identify global changes. As expected, a strong correlation exists between solvent accessible surface area changes and chemical shift changes for residues involved with inhibitor binding (annotated red in Figure 1). However, a select group of residues that are not associated with substrate interaction also display significant chemical shift perturbations. These peaks are annotated blue in Figure 1. When mapped onto the structure they arrange linearly on the interior of the C-terminal β-barrel opposite the turn/loop region Lys^{61}−Leu^{72}, which suggests that spatial reorientation with respect to this region occurs upon inhibition (Figure 6).

Interestingly, an additional number of residues (annotated green in Figure 1) display minor amide chemical shift differences between the apo and bound states. Collectively, these residues define the wider dynamic network, which extends beyond the catalytic site into the N-terminal β-barrel domain. This network appears to propagate toward regions of the protein that are involved with RNA and 3D polymerase interactions. However, chemical shift analysis between the apo and bound states indicates that although differences are observed for these flanking residues, the amino acids actually involved with RNA binding (KFRDI$^{82-86}$) do not exhibit changes upon inhibitor binding. Superposition of the RNA binding regions for number of picornaviral 3C proteases, for which both apo and inhibited forms exist (Table 2), indicates a general rigidity of the backbone within this region. These RNA binding regions superpose within 0.65 Å despite proteolytic activity or inactivation.

Global Fluctuations in Amide Hydrogen Exchange. The deuterium exchange data for the inhibited HRV14-3C protease shows that hydrogen exchange rates are uniformly distributed between the two β-barrel domains and the RNA binding site. Fifty-five of the 87 residues involved in hydrogen bonds still had signals at the end of the deuterium exchange experiment (one week following ^{1}H/^{2}H exchange). These results indicate the overall structural uniformity and relative rigidity of the inhibited enzyme (Figure 8). Not surprisingly, amides that presented the largest protection factors are located within the interior of the protein and are involved in cross β-strand hydrogen bond interactions.

In contrast, only about half the number of residues had measurable amide exchange rates for the apo enzyme following ^{1}H/^{2}H exchange. These data indicate that the C-terminal β-barrel domain undergoes faster amide exchange in the apo enzyme compared to its inhibited counterpart. Interestingly, β-strand residues Leu^{101}, Val^{102}, Cys^{151}, Ala^{152}, and Lys^{155} are spatially proximal to residues implicated in RNA binding (TGK$^{154-156}$) (*67*) and comprise the majority of C-terminal β-barrel amides for which exchange rates could be obtained.

CONCLUSION

In summary, we have solved the solution structures of both the apo and peptide-inhibitor bound HRV14-3C protease. Comparison of the inhibited HRV14-3C enzyme with its inhibited homologue (HRV2-3C) has provided a better understanding of these subgenus similarities and differences between these enzymes. The novel peptide-based inhibitor synthesized in this study revealed that some inhibitor interactions are essentially conserved across all rhinovirus subgroups, while the added length of our inhibitor provided a better understanding of downstream substrate interactions previously uncharacterized. This work also helped rationalize the extended substrate specificity noted with hydrolysis cleavage rate studies using natural 3C protease substrates (*12*−*14*, *17*).

To better understand the structural and dynamic differences between the bound and unbound states of the HRV-3C protease, the apo solution structure was solved and compared with the inhibited form. This analysis revealed that the enzyme's structure is generally similar (within 0.69 Å rmsd) between the two states. Chemical shift changes were observed for residues within the protease's C-terminal β-barrel domains that suggest minor conformational changes occur upon inhibition. The apo enzyme exhibits larger rmsd values and order parameters for regions that are involved in substrate interaction. These findings correlate with atomic displacement calculations for a homologous protease, the Polio-3C protease. Characterization of the slow time scale dynamics shows significant differences between the apo and inhibited enzyme states, which indicate that the C-terminal β-barrel domain undergoes faster amide exchange in the apo state compared to its inhibited counterpart. These results are not surprising considering that this domain is involved with proteolytic substrate recognition and cleavage. The only residues within this domain that show measurable amide exchange rates flank amino acids implicated with the virus's 3D polymerase binding. No structural change within the enzyme's RNA binding interface is observed between the apo and inhibited states. These findings raise questions as to whether structural changes in the proteolytic site may occur upon binding viral RNA. The recent structure determination of the cloverleaf RNA IRES I element that binds the 3C protease (*69*) was completed by NMR. This data provides encouragement that such protein-RNA structural studies might also be performed in solution.

ACKNOWLEDGMENT

We would like to thank the Canadian National High Field NMR Centre (NANUC) for their assistance and use of the facilities. Operation of NANUC is funded by the Canadian Institutes of Health Research, the Natural Science and Engineering Research Council of Canada, and the University of Alberta. Special thanks to M. N. G. James for providing the pET-3a HRV14-3ABC plasmid and Steve Bryson for insight and discussion regarding HRV14-3C purification.

SUPPORTING INFORMATION AVAILABLE

Synthesis details for the acetyl-LEALFQ-ethylpropenoate inhibitor and selected strip plots from the 3D ^{13}C/^{15}N-filtered/F3-edited NOESY experiment. This material is available free of charge via the Internet at http://pubs.acs.org.

REFERENCES

1. Coiras, M. T., Aguilar, J. C., Garcia, M. L., Casas, I., and Perez-Brena, P. (2004) Simultaneous detection of fourteen respiratory viruses in clinical specimens by two multiplex reverse transcription nested-PCR assays, *J Med. Virol. 72*, 484−495.
2. Hong, C. Y., Lin, R. T., Tan, E. S., Chong, P. N., Tan, Y. S., Lew, Y. J., and Loo, L. (2004) Acute respiratory symptoms in adults in general practice, *Fam. Pract. 21*, 317−323.

3. Anonymous. (2004) The common cold. NIAID fact sheet. http://www.niaid.nih.gov/factsheets/cold.htm.
4. Hughes, A. L. (2004) Phylogeny of the picornaviridae and differential evolutionary divergence of picornavirus proteins, *Infect., Genet. Evol. 4*, 143−152.
5. Clark, M. E., Hammerle, T., Wimmer, E., and Dasgupta, A. (1991) Poliovirus proteinase 3C converts an active form of transcription factor IIIc to an inactive form: a mechanism for inhibition of host cell polymerase III transcription by poliovirus, *EMBO J. 10*, 2941−2947.
6. Sharma, R., Raychaudhuri, S., and Dasgupta, A. (2004) Nuclear entry of poliovirus protease-polymerase precursor 3CD: implications for host cell transcription shut-off, *Virology 320*, 195−205.
7. Dasgupta, A. et al. (2002) *Molecular Biology of Picornaviruses* (Semler, B. L., and Wimmer, E., Ed.), ASM Press, Washington, DC.
8. Walker, P. A., Leong, L. E.-C., and Porter, A. G. (1995) Sequence and structural determinants of the interaction between the 5′-noncoding region of picornavirus RNA and rhinovirus protease 3C, *J. Biol. Chem. 270*, 14510−14516.
9. Matthews, D. A., Dragovich, P. A., Webber, S. A., Fuhrman, S. A., Patick, A. K., Zalman, L. S., Hendrickson, T. F., Love, R. A., Prins, T. J., Marakovits, J. T., Zhou, R., Tikhe., J., Ford, C. E., Meador, J. W., III, Ferre, R. A., Brown, E. L., Binford, S. L., Brothers, M. A., DeLisle, D. M., and Worland, S. T. (1999) Structure-assisted design of mechanism-based irreversible inhibitors of human rhinovirus 3C protease with potent antiviral activity against multiple rhinovirus serotypes, *Proc. Natl. Acad. Sci. U.S.A. 96*, 11000−11007.
10. Matthews, D. A., Smith, W. W., Ferre, R. A., Condon, B., Budahazi, G., Sisson, W., Villafranca, J. E., Janson, C. A., McElroy, H. E., Gribskov, C. L., and S., W. (1994) Structure of human rhinovirus 3C protease reveals a trypsin-like polypeptide fold, RNA-binding site, and means for cleaving precursor polyprotein, *Cell 77*, 761−771.
11. Johnson, T. O., Hua, Y., Luu, H. T., Brown, E. L., Chan, F., Chu, S. S., Dragovich, P. S., Eastman, B. W., Ferre, R. A., Fuhrman, S. A., Hendrickson, T. F., Maldonado, F. C., Matthews, D. A., Meador, J. W., III, Patick, A. K., Reich, S. H., Skalitzky, D. J., Worland, S. T., Yang, M., and Zalman, L. S. (2002) structure-based design of a parallel synthetic array directed toward the discovery of irreversible inhibitors of human rhinovirus 3C protease, *J. Med. Chem. 45*, 2016−2023.
12. Orr, D. C., Long, A. C., Kay, J., Dunn, B. M., and Cameron, J. M. (1989) Hydrolysis of a series of synthetic peptide substrates by the human rhinovirus 14 3C proteinase, cloned and expressed in *Escherichia coli*, *J Gen. Virol. 70*, 2931−2942.
13. Cordingley, M. G., Register, R. B., Callahan, P. L., Garskey, V. M., and Colonno, R. J. (1989) Cleavage of small peptides in vitro by human rhinovirus 14 3C protease expressed in *Escherichia coli*, *J. Virol. 63*, 5037−5045.
14. Long, A. C., Orr, D. C., Cameron, J. M., Dunn, B. M., and Kay, J. (1989) A consensus sequence for substrate hydrolysis by rhinovirus 3C protease, *FEBS Lett. 258*, 75−78.
15. Dragovich, P. S., Prins, T. J., Zhou, R., Brown, E. L., Maldonado, F. C., Fuhrman, S. A., Zalman, L. S., Tuntland, T., Lee, C. A., Patick, A. K., Matthews, D. A., Hendrickson, T. F., Kosa, M. B., Liu, B., Batugo, M. R., Gleeson, J. R., Sakata, S. K., Chen, L., Guzman, M. C., Meador, J. W., III, Ferre, R. A., and Worland, S. T. (2002) Structure-based design, synthesis, and biological evaluation of irreversible human rhinovirus 3C protease inhibitors. 6. Structure-activity studies of orally bioavailable, 2-pyridone-containing peptidomimetics, *J. Med. Chem. 45*, 1607−1623.
16. Marley, J., Lu, M., and Bracken, C. (2001) A method for efficient isotopic labeling of recombinant proteins, *J. Biomol. NMR 20*, 71−75.
17. Wang, Q. M., Johnson, R. B., Cox, G. A., Villarreal, E. C., and Loncharich, R. J. (1997) A continuous colorimetric assay for rhinovirus-14 3C protease using peptide p-nitroanilides as substrates, *Anal. Biochem. 252*, 238−245.
18. Dragovich, P. S., Webber, S. E., Babine, R. E., Fuhrman, S. A., Patick, A. K., Matthews, D. A., Lee, C. A., Reich, S. H., Prins, T. J., Marakovits, J. T., Littlefield, E. S., Zhou, R., Tikhe, J., Ford, C. E., Wallace, M. B., Meador, J. W., III, Ferre, R. A., Brown, E. L., Binford, S. L., Harr, J. E. V., DeLisle, D. M., and Worland, S. T. (1998) Structure-based design, synthesis, and biological evaluation of irreversible human rhinovirus 3C protease inhibitors. 1. Michael acceptor structure-activity studies, *J. Med. Chem. 41*, 2806−2818.
19. Wishart, D. S., Bigam, C. G., Yao, J., Abildgaard, F., Dyson, H. J., Oldfield, E., Markley, J. L., and Sykes, B. D. (1995) ^{1}H, ^{13}C and ^{15}N chemical shift referencing in biomolecular NMR, *J. Biomol. NMR 6*, 135−140.
20. Ikura, M., Kay, L. E., and Bax, A. (1990) A novel approach for sequential assignment of ^{1}H, ^{13}C and ^{15}N spectra of larger proteins: Heteronuclear triple-resonance three-dimensional NMR spectroscopy. Application to calmodulin, *Biochemistry 29*, 4659−4667.
21. Wittekind, M., and Mueller, L. (1993) HNCACB, a High-sensitivity 3D NMR experiment to correlate amide-proton and nitrogen resonances with the alpha and beta-carbon resonances in proteins, *J. Magn. Reson. B 101*, 201−205.
22. Grzesiek, S., and Bax, A. (1992) correlating backbone amide and side chain resonances in larger proteins by multiple relayed triple resonance NMR, *J. Am. Chem. Soc. 114*, 6291−6293.
23. Grzesiek, S., Anglister, J., and Bax, A. (1993) Correlation of backbone amide and aliphatic side-chain resonances in ^{13}C/^{15}N-enriched proteins by isotropic mixing of ^{13}C magnetization, *J. Magn. Reson. B 101*, 114−119.
24. Muhandiram, D. R., and Kay, L. E. (1994) Gradient-enhanced triple-resonance 3-dimensional NMR experiments with improved sensitivity, *J. Magn. Reson. B 103*, 203−216.
25. Bax, A., Clore, G. M., and Gronenborn, A. M. (1990) ^{1}H-^{1}H correlation *via* isotropic mixing of ^{13}C magnetization, a new 3-dimensional approach for assigning ^{1}H and ^{13}C spectra of ^{13}C-enriched proteins, *J. Magn. Reson. 88*, 425−431.
26. Kay, L. E., Xu, G. Y., Singer, A. U., Muhandiram, D., and Forman-Kay, J. D. (1993) A gradient-enhanced HCCH-TOCSY experiment for recording side-chain ^{1}H and ^{13}C correlations in H_2O samples of proteins, *J. Magn. Reson. B 101*, 333−337.
27. Vuister, G. W., and Bax, A. (1993) Quantitative J correlation: A new approach for measuring homonuclear three-bond J(HNHα) coupling constants in ^{15}N-enriched proteins, *J. Am. Chem. Soc. 115*, 7772−7777.
28. Bjorndahl, T. C., Monzavi, H., and Wishart, D. S. (2003) Letter to the editor: Backbone ^{1}H, ^{15}N and ^{13}C assignments for the human rhinovirus 3C protease (serotype 14), *J. Biomol. NMR 26*, 85−86.
29. Kay, L. E., Keifer, P., and Saarinen, T. (1992) Pure absorption gradient enhanced heteronuclear single quantum correlation spectroscopy with improved sensitivity, *J. Am. Chem. Soc. 114*, 10663−10665.
30. Zhang, O., Kay, L. E., Olivier, J. P., and Forman-Kay, J. D. (1994) Backbone ^{1}H and ^{15}N resonance assignments of the N-terminal SH3 domain of DRK in folded and unfolded states using enhanced-sensitivity pulsed field gradient NMR techniques, *J. Biomol. NMR 4*, 845−858.
31. Delaglio, F., Grzesiek, S., Vuister, G. W., Zhu, G., Pfeifer, J., and Bax, A. (1995) NMRPipe: a multidimensional spectral processing system based on UNIX pipes, *J. Biomol. NMR 6*, 277−293.
32. Johnson, B. A., and Blevins, R. B. (1994) NMRView: A computer program for the visualization and analysis of NMR data, *J. Biomol. NMR 4*, 603−614.
33. Ikura, M., and Bax, A. (1992) Isotope-filtered 2D NMR of a protein-peptide complex: study of a skeletal muscle myosin light chain kinase fragment bound to calmodulin, *J. Am. Chem. Soc. 114*, 2433−2440.
34. Zwahlen, C., Legault, P., Vincent, S. J. F., Greenblatt, J., Konrat, R., and Kay, L. E. (1997) Methods for measurement of intermolecular NOEs by multinuclear NMR spectroscopy: application to a bacteriophage lambda N-peptide/BoxB RNA complex, *J. Am. Chem. Soc. 119*, 6711−6721.
35. Cornilescu, G., Delaglio, F., and Bax, A. (1999) Protein backbone angle restraints from searching a database for chemical shift and sequence homology, *J. Biomol. NMR 13*, 289−302.
36. Neal, S., Berjanskii, M., Zhang, H., and Wishart, D. S. (2006) Accurate prediction of protein torsion angles using chemical shifts and sequence homology. *Magn. Reson. Chem. 44*, S158−67.
37. Schwieters, C. D., Kuszewski, J. J., Tjandra, N., and Clore, G. M. (2003) The Xplor-NIH NMR molecular structure determination package, *J. Magn. Reson. 160*, 65−73.
38. Brunger, A. T., and Adams, P. D., and Clore, G. M., and DeLano, W. L., and Gros, P., and Grosse-Kunstleve, R. W., and Jiang, J. S., and Kuszewski, J., and Nilges, M., and Pannu, N. S., and Read R. J., and Rice, L. M., and Simonson, T., and Warren, G. L. (1998) Crystallography & NMR system: A new software suite for

macromolecular structure determination, *Acta Crystallogr., Sect. D: Biol. Crystallogr. 54*, 905−921.
39. Nederveen, A. J., Doreleijers, J. F., Vranken, W., Miller, Z., Spronk, C. A. E. M., Nabuurs, S. B., Guentert, P., Livny, M., Markley, J. L., Nilges, M. L. U. E., Kaptein, R., and Bonvin, A. M. (2005) RECOORD: A recalculated coordinate database of 500+ proteins from the PDB using restraints from the BioMagResBank, *Proteins 59*, 662−672.
40. Güntert, P., Mumenthaler, C., and Wüthrich, K. (1997) Torsion angle dynamics for NMR structure calculation with the new program DYANA, *J. Mol. Biol. 273*, 283−298.
41. Herrmann, T., Güntert, P., and Wüthrich, K. (2002) Protein NMR structure determination with automated NOE assignment using the new software CANDID and the torsion angle dynamics algorithm DYANA, *J. Mol. Biol. 319*, 209−227.
42. Mumenthaler, C., Güntert, P., Braun, W., and Wüthrich, K. (1997) Automated combined assignment of NOESY spectra and three-dimensional protein structure determination, *J. Biomol. NMR 10*, 351−362.
43. Mosimann, S. C., Cherney, M. M., Sia, S., Plotch, S., and James, M. N. G. (1997) Refined X-ray crystallographic structure of the poliovirus 3C gene product, *J. Mol. Biol. 273*, 1032−1047.
44. Birtley, J. R., Knox, S. R., Jaulent, A. M., Brick, P., Leatherbarrow, R. J., and Curry, S. (2005) Crystal structure of foot-and-mouth disease virus 3C protease. New insights into catalytic mechanism and cleavage specificity, *J. Biol. Chem. 280*, 11520−11527.
45. Boyko, R., and Sykes, B. (1994) XCRVFIT: A graphical X-windows program for binding curve studies and NMR spectroscopic analysis. http://www.bionmr.ualberta.ca/bds/software/xcrvfit.
46. Bai, Y., Milne, J. S., Mayne, L., and Englander, S. W. (1993) Primary structure effects on peptide group hydrogen exchange, *Proteins 17*, 75−86.
47. Connelly, G. P., Bai, Y., Jeng, M., and Englander, S. (1993) Isotope effects in peptide group hydrogen exchange, *Proteins 17*, 87−92.
48. Wang, Q. M. and Johnson, R. B. (2001) Activation of human rhinovirus-14 3C protease, *Virology 280*, 80−86.
49. Doreleijers, J., Raves, M., Rullmann, J., and Kaptein, R. (1999) Completeness of NOEs in protein structure: A statistical analysis of NMR, *J. Biomol. NMR 14*, 123−132.
50. Laskowski, R. A., MacArthur, M. W., Moss, D. S., and Thorton, J. M. (1993) PROCHECK: A program to check the stereochemical quality of protein structures, *J. Appl. Crystallogr. 26*, 283−290.
51. Willard, L., Ranjun, A., Zhang, H., Monzavi, H., Boyko, R. F., Sykes, B. D., and S. W. D. (2003) VADAR: A web server for quantitative evaluation of protein structure quality, *Nucleic Acids Res. 31*, 3316−3319.
52. Hooft, R. W. W., Vriend, G., Sander, C., and Abola, E. E. (1996) Errors in protein structures, *Nature 381*, 272.
53. Wüthrich, K. (1986) *NMR of Proteins and Nucleic acids*, Wiley Press, New York, NY.
54. Montelione, G. T., Wüthrich, K., Nice, E. C., Burgess, A. W., and Scheraga, H. A. (1986) Identification of two anti-parallel beta-sheet conformations in the solution structure of murine epidermal growth factor by proton magnetic resonance, *Proc. Natl. Acad. Sci. U.S.A. 83*, 8594−8598.
55. Pardi, A., Billeter, M., and Wüthrich, K. (1984) Calibration of the angular dependence of the amide proton-C_α proton coupling constants, ^{3}J-HNHα, in a globular protein. Use of ^{3}J-HNHα for identification of helical secondary structure, *J. Mol. Biol. 180*, 741−751.
56. Wishart, D. S., Sykes, B. D., and Richards, F. M. (1992) The chemical shift index: A fast and simple method for the assignment of protein secondary structure through NMR spectroscopy, *Biochemistry 31*, 1647−1651.
57. Dragovich, P. S., Prins, T. J., Zhou, R., Fuhrman, S. A., Patick, A. K., Matthews, D. A., Ford, C. E., Meador, J. W., Ferre, R. A., and Worland, S. T., III (1999) Structure-based design, synthesis, and biological evaluation of irreversible human rhinovirus 3C protease inhibitors. 3. Structure-activity studies of ketomethylene-containing peptidomimetics, *J. Med. Chem. 42*, 1203−1212.
58. Binford, S. L., Maldonado, M. A., Brothers, P. T., Weady, L. S., Zalman, J. W., Meador, D. A., and Patick, A. K., III (2005) Conservation of amino acids in human rhinovirus 3C protease correlates with broad-spectrum antiviral activity of Rupintrivir, a novel human rhinovirus 3C protease inhibitor, *Antimicrob. Agents Chemother. 49*, 619−626.
59. Lavigne, P., Bagu, J. R., Boyko, R., Willard, L., Holmes, C. F., and Sykes, B. D. (2000) Structure-based thermodynamic analysis of the dissociation of protein phosphatase-1 catalytic subunit and microcystin-LR docked complexes, *Protein Sci. 9*, 252−264.
60. Cox, G. A., Johnson, R. B., Cook, J. A., Wakulchik, M., Johnson, M. G., Villarreal, E. C., and Wang, Q. M. (1999) Identification and characterization of human rhinovirus-14 3C protease deamidation isoform, *J. Biol. Chem. 274*, 13211−13216.
61. Geiger, T., and Clarke, S. (1987) Deamidation, isomerization and racemization at asparaginyl and aspartyl residues in peptides. Succinimide-linked reactions that contribute to protein degradation, *J. Biol. Chem. 262*, 785−794.
62. DeLano, W. L. (2002) DeLano Scientific, San Carlos, CA.
63. Billeter, M., Kline, A. D., Braun, W., Huber, R., and Wüthrich, K. (1989) Comparison of the high-resolution structures of the alpha-amylase inhibitor tendamistat determined by nuclear magnetic resonance in solution and by X-ray diffraction in single crystals, *J. Mol. Biol. 206*, 677−687.
64. Billeter, M. (1992) Comparison of protein structures determined by NMR in solution and by X-ray diffraction in single crystals, *Q. Rev. Biophys. 25*, 325−377.
65. Berjanskii, M. V., and Wishart, D. S. (2005) A simple method to predict protein flexibility using secondary chemical shifts, *J. Am. Chem. Soc. 127*, 14970−14971.
66. Tjandra, N., and Bax, A. (1997) Solution NMR measurement of amide proton chemical shift anisotropy in ^{15}N-enriched proteins. Correlation with hydrogen bond length, *J. Am. Chem. Soc. 119*, 8076−8082.
67. Shih, S.-R., Chiang, C., Chen, T.-C., Wu, C.-N., Hsu, J. T.-A., Lee, J.-C., Hwang, M.-J., Li, M.-L., Chen, G.-W., and Ho, M.-S. (2004) Mutations at KFRDI and VGK domains of enterovirus 7C protease affect its RNA binding and proteolytic activities, *J. Biomed. Science 11*, 239−248.
68. Andino, R., Rieckhof, G. E., Achacoso, P. L., and Baltimore, D. (1993) Poliovirus RNA synthesis utilizes an RNP complex formed around the 5′-end of viral RNA, *EMBO J. 12*, 3587−3598.
69. Du, Z., Yu, J., Ulyanov, N. B., and James, T. L. (2004) Solution structure of a consensus stem-loop D RNA domain that plays important roles in regulation, translation and replication in enteroviruses and rhinoviruses, *Biochemistry 43*, 11959−11972.
70. Koradi, R., Billeter, M., and Wüthrich, K. (1996) MOLMOL: A program for display and analysis of macromolecular structures, *J. Mol. Graphics 14*, 51−55.
71. Wallace, A. C., Laskowski, R. A., and M. T. J. (1995) LIGPLOT: A program to generate schematic diagrams of protein-ligand interactions, *Protein Eng. 8*, 127−134.

BI7010866